

Disentangling the optical AGN and Host-galaxy luminosity with a probabilistic Flux Variation Gradient^{★,★★}

N. Gianniotis¹, F. Pozo Nuñez¹, and K. L. Polsterer¹

Astroinformatics, Heidelberg Institute for Theoretical Studies, Schloss-Wolfsbrunnenweg 35, 69118 Heidelberg, Germany
e-mail: nikos.gianniotis@h-its.org

Received ??, 2021; accepted ??, 2021

ABSTRACT

Context. We present a novel Probabilistic Flux Variation Gradient (PFVG) approach to disentangle the active galactic nuclei (AGN) and host-galaxy contributions in the context of photometric reverberation mapping (PRM) of AGN.

Aims. We explored the ability to recover the fractional contribution, in a model-independent way, by using simultaneously the entire set of light curves obtained through different filters and photometric apertures.

Methods. The method is based on the observed "bluer when brighter" phenomena attributed to the superimposition of a two component structure; the red-host galaxy, which is constant in time, and the varying blue AGN. We describe the PFVG mathematical formalism and demonstrate its performance using simulated light curves and available PRM observations.

Results. The new probabilistic approach is able to recover host-galaxy fluxes within 1% precision, as long as the light curves do not show a significant contribution from time-delays. This represent a significant improvement with respect to previous applications of the traditional FVG method on PRM data.

Conclusions. The proposed PFVG provides an efficient and accurate way to disentangling the AGN and host-galaxy luminosities in PRM monitoring data. The method will be specially helpful in the case of large upcoming photometric survey telescopes like the LSST. Finally, we have made the algorithms freely available as part of our *Julia* PFVG package.

Key words. galaxies: active –galaxies: quasars –galaxies: nuclei –galaxies: Seyfert

1. Introduction

Powered by supermassive black holes in their centers, active galactic nuclei (AGN) are considered to be the most energetic sources in the Universe. The physical regions involved are extremely compact to be resolved with existing instrumentation. As a result, AGN often appear as a point-like source compared with its host-galaxy, which can have an ample variety of morphologies (e.g.; Gabor et al. 2009; Villforth et al. 2014), and whose degree of contribution to the total flux varies significantly (e.g.; Pierce et al. 2010; Pović et al. 2012; Falomo et al. 2014; Bettoni et al. 2015).

Particularly challenging is the case of local Seyfert galaxies where the starlight contribution can reach up to 50 to ~80% of the total optical (e.g.; Bentz et al. 2009; Sakata et al. 2010; Pozo Nuñez et al. 2012; 2013) and infrared luminosities (e.g.; Glass 1998; Glass 2004; Suganuma et al. 2006; Pozo Nuñez et al. 2014; 2015; Koshida et al. 2014). An overestimation of the AGN luminosity due to the contamination of its host-galaxy has strong implications on the refinement of scaling relations for single-epoch black hole estimations, such as the H β broad-line region (BLR) size - 5100 Å monochromatic luminosity relation ($R_{\text{BLR}} \propto L_{\text{AD}}^\alpha$; Bentz et al. 2013). The $R_{\text{BLR}} \propto L_{\text{AD}}^\alpha$ relation offers the possibility of using quasars as standard candles for cosmological distance studies (Oknyanskij 1999; Watson et al. 2011). However, this can only be achieved if the scatter is reduced

considerably. The scatter in this relation appears not only because of the noise in time delay measurements, from which BLR sizes are inferred, but also from erroneous disentangling of AGN and host galaxy luminosities. This has been demonstrated by Bentz et al. (2013) who obtained an improved slope of $\alpha = 0.533^{+0.035}_{-0.033}$ for a sample of 41 reverberation-mapped Seyfert-1 galaxies after correcting for starlight contamination.

To date, there are two main methods for isolating nuclear flux: fitting galaxy templates to the observed AGN spectrum (e.g.; Mehdipour et al. 2015), and modeling the host-galaxy profile using high-resolution images (e.g.; Pogge & Martini 2002; Bentz et al. 2009, 2013, using Hubble Space Telescope – HST imaging). The first method can be directly applied to spectroscopic reverberation mapping (SRM) campaigns, while the second is mostly restricted to local Seyfert galaxies where the host-galaxy is optically resolved, and depends strongly on the galaxy model adopted. However, neither method is efficient in the case of large monitoring programs, in particular, in the case of large scale photometric reverberation mapping (PRM) surveys. This raises a practical concern regarding the processing of the unprecedented amount of data that will be provided by large ground based photometric surveys (LSST; LSST Science Collaboration et al. 2009, SDSS-V; Kollmeier et al. 2019), and satellite missions (TESS; Jenkins et al. 2018, JWST; Natarajan et al. 2017, Euclid; Amendola et al. 2018) in the near future.

An alternative approach, which does not require the use of high spatial resolution images, is the flux variation gradient method (FVG, Winkler et al. 1992; Glass 1997; Glass 1998). The FVG is based on the flux-flux diagrams by Choloniewski (1981), who attributed the observed "bluer when brighter" phe-

[★] The PFVG code can be downloaded from: <https://github.com/HITS-AIN/ProbabilisticFluxVariationGradient.jl/>

^{★★} Instructions and specific examples used in this paper can be found in: https://github.com/HITS-AIN/PFVG_AA2021

nomena to the superimposition of a two-component structure: the constant in time contribution of a red host-galaxy, including non-varying emission lines, and the varying contribution of an AGN with constant blue color.

Recently, given a well defined range of host-galaxy slopes (e.g. Sakata et al. 2010), the FVG has been successfully employed in disentangling host and AGN contributions in narrow and broad-band PRM campaigns (e.g.; Pozo Nuñez et al. 2012; Ramolla et al. 2015; Pozo Nuñez et al. 2019; Chelouche et al. 2019), as well as in dust near-infrared RM studies (e.g.; Pozo Nuñez et al. 2014; 2015; Vazquez et al. 2015; Ramolla et al. 2018). However, its actual application has considerable difficulties and limitations which have not yet been fully addressed and quantified. For instance, can a FVG analysis give a reliable estimate of the host-galaxy contribution based solely on traditional linear regression analysis? Or will it rather return biased results given the observational errors in the data, different amplitudes and variability features in the light curves? To what degree are FVGs affected by light curves with time-delays obtained from PRM observations? To answer these questions in this paper, we study the reliability of the FVG method under different observational conditions, and introduce a new probabilistic approach which can be efficiently applied to PRM monitoring data.

2. Methods

In the following section we briefly revisit the FVG method and introduce a new probabilistic reformulation. We note that a review of the FVG method and its application to PRM data can be found in Pozo Nuñez et al. (2012). Here we list the formulae and principle for the sake of comprehensiveness.

2.1. On the flux variation gradient

The purpose of FVG is to disentangle the AGN and host-galaxy contributions given the observed total flux and a ratio of colours characterising the host-galaxy in question. Observed total fluxes $y_i(t)$ are the sum of a constant in time host-galaxy flux $g_i(t) = g_i$ and the variable AGN flux $v_i(t)$:

$$y_i(t) = v_i(t) + g_i. \quad (1)$$

There are two assumptions that underpin the FVG method. The first assumption is that the AGN fluxes $v_i(t)$ form a line that goes through the origin. The second assumption, supported by observations, is that total fluxes $y_i(t)$ obtained through different photometric bands $i \in \{1, \dots, F\}$, where F is the total number of filters, follow a linear relationship. The AGN optical spectral shape does not change, i.e. the ratio $\frac{v_i(t)}{v_j(t)} = \Gamma_{ij}$ is a constant known as the flux variation gradient by Winkler et al. (1992). Hence, we can write the assumption of a linear relationship as:

$$y_i(t) = \Gamma_{ij} y_j(t) + g_i - \Gamma_{ij} g_j. \quad (2)$$

Figure 1 sketches the FVG method. On the right hand side we see observations in two different filters. By pairing flux values of observations that occur at the same time, we form points $(y_i(t), y_j(t))$ in the flux-flux plot that fall on the dashed line, as dictated by Equation (2). Each of the instantiated points $(y_i(t), y_j(t))$ in the flux-flux plot can be understood as a vector that results from adding the unobserved AGN vector $(v_i(t), v_j(t))$ (not plotted in Fig. 1) to the unobserved galaxy vector $\mathbf{g}_{ij} = (g_i, g_j)$ (brown vector in Fig. 1), as implied by Equation (1). Obviously, if we knew the galaxy vector \mathbf{g}_{ij} , we

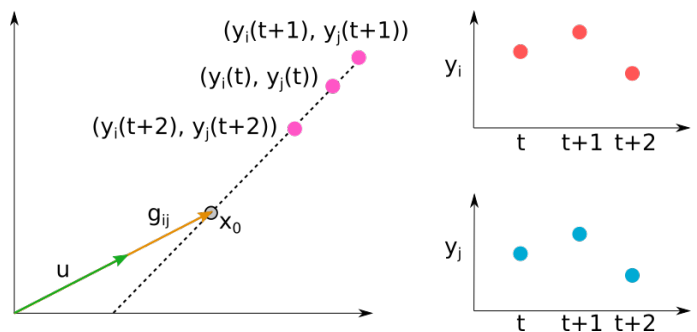


Fig. 1. Sketch of FVG: on the right hand side, we see observations in filters i and j measured at three different time instances. By pairing flux values of co-occurring observations, we form points in the flux-flux plot that fall on a line (dashed). Vector \mathbf{g}_{ij} (in brown) corresponds to the unobserved host-galaxy and defines a line $\mathbf{g}_{ij} \cdot x$ that intersects the dashed line at x_0 , the point of (unobserved) minimum AGN activity. The FVG method consists in finding the intersection of $\mathbf{u} \cdot x$ and the dashed line; \mathbf{u} (in green) is a vector that has the same direction (i.e. same colours) as \mathbf{g}_{ij} and therefore intersects the dashed line also at x_0 .

could subtract it from the observed $(y_i(t), y_j(t))$ and obtain the desired AGN activity $(v_i(t), v_j(t))$. The unobserved vector \mathbf{g}_{ij} defines a line $\mathbf{g}_{ij} \cdot x$, with $x \in \mathbb{R}$, that intersects the dashed line in Figure 1 at point $x_0 \in \mathbb{R}^2$, which stands for the (not necessarily observed) minimum AGN activity at filters i and j . Hence, if we can find x_0 , then we know \mathbf{g}_{ij} . The FVG method suggests the following: if we knew a vector \mathbf{u} with the same direction as \mathbf{g}_{ij} , this would define the line $\mathbf{u} \cdot x$ which is just a reparametrisation of the line $\mathbf{g}_{ij} \cdot x$. Hence, the intersection of the line $\mathbf{u} \cdot x$ with the dashed line would also occur at x_0 which would give us \mathbf{g}_{ij} . In a nutshell, FVG proposes that if we know the ratio of colours characterising the host galaxy in question, then we can find the point x_0 and disentangle the AGN and host galaxy luminosities.

In practical implementations of the FVG, the lines describing the total fluxes are identified using linear regression analysis. As pointed out in Pozo Nuñez et al. (2012), the choice of the regression method is not trivial as the methods will fare differently depending on how well separated the dependent and independent variables are, the intrinsic dispersion of data around the best fit and others factors (e.g., Isobe et al. 1990; Winkler et al. 1992). The regression algorithms are based on the formulae provided by Isobe et al. (1990). The authors recommend a symmetric treatment of the variables using the ordinary least squares (OLS) bisector method. A mean host-galaxy estimate is obtained from a random uniform distribution of possible host-galaxy values enclosed by the area formed by the intersection between a well defined range of host-galaxy colors¹ and the AGN slopes derived from the bisector analysis.

2.2. Issues with past FVG implementations

Aggregating filters: As illustrated in Figure 1, the FVG works on a flux-flux plot, defined by a pair of filters, and finds an intersection point $x_0 \in \mathbb{R}^2$. This is repeated for each pair of filters and the resulting intersection points are then aggregated in some fashion or considered independently. In previous applications of the FVG, aggregation of the intersection points per filter pair has been done by averaging estimates (e.g. Pozo Nuñez et al. 2012; Ramolla et al. 2015; Chelouche et al. 2019). Here we

¹ PRM studies typically consider the host-galaxy slopes given by Sakata et al. (2010) obtained for 11 Seyfert-1 galaxies.

avoid this heuristic aggregation by considering all filters simultaneously to infer \mathbf{x}_0 . Hence, instead of working in a flux-flux space that contains information about two filters only, we work in the F -dimensional space of all filters (i.e. each filter has an axis) populated by tuples $(y_1(t), \dots, y_F(t))$, and infer an intersection point $\mathbf{x}_0 \in \mathbb{R}^F$.

Data uncertainty: The linear regression algorithms used in the past, e.g., OLS bisector, assume that the intrinsic dispersion of the data is larger than individual error measurements, hence the intersection point between the AGN and galaxy slopes, i.e. the host-galaxy, depends solely on the error range of the bisector fit. In this work, we account for the presence of noise on the data by explicitly taking error measurements into account in our model formulation (see Section 2.3).

Uncertainty in the galaxy estimation: Previous FVG implementations provide point estimates for the intersection points and hence the galaxy contribution. By formulating a probabilistic version of FVG in this work, we are able to produce not just a point estimate for the intersection point but rather a density of possible intersection points (see Section 2.3.2). This density expresses our inability to pinpoint a unique intersection point due to the presence of noise (i.e. uncertainty) in the observed data, and acknowledges that a range of solutions are in fact plausible.

2.3. Proposed probabilistic FVG

In this section we put forward a probabilistic reformulation of FVG based on probabilistic principal component analysis (PPCA; Tipping and Bishop 1999) which we call PFVG. In a first step, our method identifies the line formed by the total fluxes, and in a second step, it seeks the intersection of the unobserved galaxy line with the identified line.

We model the observed flux $y_i(t)$ in each filter $i \in \{1, \dots, F\}$, at time t , as a noisy observation from a latent signal $f(t)$ ², common to all filters, scaled and shifted by filter-dependent parameters a_i and b_i :

$$y_i(t) = a_i f(t) + b_i + \epsilon_i(t), \quad i \in \{1, \dots, F\}, \quad (3)$$

where $\epsilon_i(t)$ is observational noise assumed to be drawn from a Gaussian distribution, $\epsilon_i(t) \sim \mathcal{N}(0, \sigma^2(t))$. This incorporates the FVG assumption that a flux observation in a filter at time t , is linearly related to the observations in all other filters at time t . Assuming observations co-occur, i.e. they are observed at the same time instance, we form vectors $\mathbf{y}(t) = (y_1(t), y_2(t), \dots, y_F(t)) \in \mathbb{R}^F$ for each observed t . Similarly, we also form $\boldsymbol{\sigma}^2(t) = (\sigma_1(t), \sigma_2(t), \dots, \sigma_F(t))$.

2.3.1. Line Identification

The co-occurring, noisy observed total fluxes in Eq. 3 gives rise to the joint likelihood³:

$$p(D|\mathbf{a}, \mathbf{b}, \mathbf{f}) = \prod_t \mathcal{N}(\mathbf{y}(t)|\mathbf{a}f(t) + \mathbf{b}, \boldsymbol{\sigma}^2(t)\mathbf{I}), \quad (4)$$

² In the context of this work the latent signal $f(t)$ correspond to the driving AGN continuum light curves modelled as random walk in Section 3.

³ \mathbf{I} stands for the identity matrix. Its dimensions are implicitly defined by its context, e.g. in Eq. 4 it is of dimensions $F \times F$.

where $\mathbf{a} = (a_1, \dots, a_F)$, $\mathbf{b} = (b_1, \dots, b_F)$ and D stands for all observed measurements, i.e. all available data. The proposed model seeks to find the line that goes through the observed total fluxes. It is essentially identical to PPCA in the special case where only one principal component is sought. Since, we are not interested in the latent signal values $f(t)$, we treat them as ‘nuisance’ variables: following PPCA, we impose on them a Gaussian prior $\mathcal{N}(\mathbf{f}|\mathbf{0}, \mathbf{I}) = \prod_t \mathcal{N}(f(t)|0, 1)$ and integrate them out:

$$\begin{aligned} p(D|\mathbf{a}, \mathbf{b}) &= \int \prod_t \mathcal{N}(\mathbf{y}(t)|\mathbf{a}f(t) + \mathbf{b}, \boldsymbol{\sigma}^2(t)\mathbf{I}) \mathcal{N}(\mathbf{f}|\mathbf{0}, \mathbf{I}) d\mathbf{f} \\ &= \prod_t \mathcal{N}(\mathbf{y}(t)|\mathbf{b}, \mathbf{a}\mathbf{a}^T + \boldsymbol{\sigma}^2(t)\mathbf{I}). \end{aligned} \quad (5)$$

Maximising $p(D|\mathbf{a}, \mathbf{b})$ in Equation 5 with respect to line parameters \mathbf{a} and \mathbf{b} gives us point estimates for these parameters. However, we want to obtain a posterior density for these parameters because we are interested in the uncertainty of our estimates. Following Bayesian principal component analysis (Bishop 1999a; Bishop 1999b), we treat \mathbf{a} and \mathbf{b} as random variables and impose priors $\mathcal{N}(\mathbf{a}|\mathbf{0}, \nu_\alpha \mathbf{I})$ and $\mathcal{N}(\mathbf{b}|\mathbf{0}, \nu_\beta \mathbf{I})$ ⁴. We now seek to obtain the posterior density $p(\mathbf{a}, \mathbf{b}|D) \propto p(D|\mathbf{a}, \mathbf{b})p(\mathbf{a})p(\mathbf{b})$.

Unfortunately, the posterior density $p(\mathbf{a}, \mathbf{b}|D)$ cannot be calculated analytically. Instead, we seek a Gaussian approximating posterior $\mathcal{N}(\mathbf{a}, \mathbf{b}|\boldsymbol{\mu}, \boldsymbol{\Sigma})$ that is as ‘close’ as possible to the exact posterior $p(\mathbf{a}, \mathbf{b}|D)$ (Bishop 1999b). An appropriate notion of ‘closeness’ is given by the Kullback-Leibler divergence between the two densities, $D_{KL}(\mathcal{N}(\mathbf{a}, \mathbf{b}|\boldsymbol{\mu}, \boldsymbol{\Sigma})||p(\mathbf{a}, \mathbf{b}|D))$. By minimizing this divergence with respect to the free parameters $\boldsymbol{\mu}$ and $\boldsymbol{\Sigma}$, we obtain the optimal (i.e. ‘closest’) Gaussian approximation to $p(\mathbf{a}, \mathbf{b}|D)$.

2.3.2. Intersection

The Gaussian approximating posterior $\mathcal{N}(\mathbf{a}, \mathbf{b}|\boldsymbol{\mu}, \boldsymbol{\Sigma})$ presents not just a single solution for the parameters of the line formed by the total fluxes, but rather a density of possible parameter solutions and hence a density of possible lines. Our goal here is to work out the density of intersection \mathbf{x}_0 between a given candidate line $\mathbf{u} \cdot \mathbf{x}$ for the unobserved galaxy and the density of lines implied by $\mathcal{N}(\mathbf{a}, \mathbf{b}|\boldsymbol{\mu}, \boldsymbol{\Sigma})$.

While the term intersection has a clear meaning for two lines that live in a Euclidean space, we still need to clarify what we mean by it in our setting. We consider a point \mathbf{x}_0 to be an intersection if it satisfies simultaneously two conditions, namely: (1) it is close to the line $\mathbf{u} \cdot \mathbf{x}$, and (2) it is close to a line $\mathbf{a} \cdot t + \mathbf{b}$ that enjoys high density according to $\mathcal{N}(\mathbf{a}, \mathbf{b}|\boldsymbol{\mu}, \boldsymbol{\Sigma})$. Allowing momentarily for some noise tolerance ς and ϱ , we express the joint satisfaction of these two conditions as the product $\mathcal{N}(\mathbf{x}_0|\mathbf{u} \cdot \mathbf{x}, \varsigma^2) \cdot \mathcal{N}(\mathbf{x}_0|\mathbf{a} \cdot t + \mathbf{b}, \varrho^2)$ where each term respectively stands for conditions (1) and (2). Noise ς and ϱ control how close \mathbf{x}_0 must be to the two lines in order to be considered an intersection. Hence, we view the two terms as soft constraints that need to be satisfied. By driving ς to 0, the first constraint becomes a hard constraint that states that \mathbf{x}_0 must be on the line $\mathbf{u} \cdot \mathbf{x}$. Roughly speaking, the product now becomes $\lim_{\varsigma \rightarrow 0} \mathcal{N}(\mathbf{x}_0|\mathbf{u} \cdot \mathbf{x}, \varsigma^2 \mathbf{I}) \mathcal{N}(\mathbf{x}_0|\mathbf{a} \cdot t + \mathbf{b}, \varrho^2 \mathbf{I}) = \mathcal{N}(\mathbf{u} \cdot \mathbf{x}|\mathbf{a} \cdot t + \mathbf{b}, \varrho^2 \mathbf{I})$.

Hence, given \mathbf{a} , \mathbf{b} and t , the conditional support for $\mathbf{u} \cdot \mathbf{x}$ being an intersection point, or equivalently, the conditional support for coordinate⁵ x addressing an intersection point is $p(x|\mathbf{a}, \mathbf{b}, t) =$

⁴ In all numerical experiments we use $\nu_\alpha = \nu_\beta = 10^{-4}$.

⁵ Coordinate x addresses a unique point on the line $\mathbf{u} \cdot \mathbf{x}$.

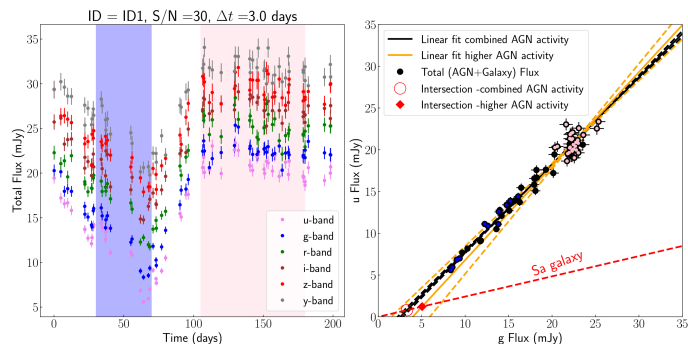


Fig. 2. Flux variation gradient applied on set of light curves from our LSST mock catalogue. The left panel shows the light curves with an average time sampling of $\Delta t = 3$ days, $S/N = 30$, and total time span of $T = 200$ days. Low and high levels of AGN activity are marked with blue and magenta colored boxes respectively. The right panel shows the FVG analysis for the u and g -bands only. Other bands are given in the Appendix in Figure A.2. The dotted orange and black lines covers the upper and lower standard deviations of the OLS bisector fit (solid lines) for the combined (black) and higher (orange) AGN state of activity. The color of the Sa galaxy used in the simulations is shown as a red dotted line.

$N(\mathbf{u} \cdot \mathbf{x} | \mathbf{a} \cdot \mathbf{t} + \mathbf{b}, \varrho^2 \mathbf{I})$. Assuming the improper prior⁶ $p(t) \propto 1$, the unconditional support for x is:

$$\begin{aligned} p(x) &\propto \int \int \int p(x | \mathbf{a}, \mathbf{b}, t) N(\mathbf{a}, \mathbf{b} | \boldsymbol{\mu}, \boldsymbol{\Sigma}) p(t) d\mathbf{a} d\mathbf{b} dt \\ &= \int \int \int N(\mathbf{u} \cdot \mathbf{x} | \mathbf{a} \cdot \mathbf{t} + \mathbf{b}, \varrho^2 \mathbf{I}) N(\mathbf{a}, \mathbf{b} | \boldsymbol{\mu}, \boldsymbol{\Sigma}) p(t) d\mathbf{a} d\mathbf{b} dt. \end{aligned} \quad (6)$$

Specifying the following partitions of mean and covariance:

$$\boldsymbol{\mu} = \begin{pmatrix} \boldsymbol{\mu}_a \\ \boldsymbol{\mu}_b \end{pmatrix}, \quad \boldsymbol{\Sigma} = \begin{pmatrix} \boldsymbol{\Sigma}_{aa} & \boldsymbol{\Sigma}_{ab} \\ \boldsymbol{\Sigma}_{ba} & \boldsymbol{\Sigma}_{bb} \end{pmatrix}, \quad (7)$$

as well as $\boldsymbol{\Sigma}_{a|b} = \boldsymbol{\Sigma}_{aa} - \boldsymbol{\Sigma}_{ab} \boldsymbol{\Sigma}_{bb}^{-1} \boldsymbol{\Sigma}_{ba}$, integration over \mathbf{a} and \mathbf{b} yields:

$$p(x) \propto \int N(\mathbf{u} \cdot \mathbf{x} | \boldsymbol{\mu}_a \cdot \mathbf{t} + \boldsymbol{\mu}_b, \varrho^2 \mathbf{I} + \boldsymbol{\Sigma}_{a|b} \mathbf{t} \mathbf{t}^T + \mathbf{R}(t) \boldsymbol{\Sigma}_{bb} \mathbf{R}(t)^T) p(t) dt. \quad (8)$$

where we have defined $\mathbf{R}(t) = \boldsymbol{\Sigma}_{ab} \boldsymbol{\Sigma}_{bb}^{-1} \mathbf{t} + \mathbf{I}$. Again, by driving noise ϱ to 0, we finally arrive to the support for x given by the density of lines implied by $N(\mathbf{a}, \mathbf{b} | \boldsymbol{\mu}, \boldsymbol{\Sigma})$ in the absence of noise (i.e. $\varsigma = \varrho = 0$)⁷:

$$p(x) \propto \int N(\mathbf{u} \cdot \mathbf{x} | \boldsymbol{\mu}_a \cdot \mathbf{t} + \boldsymbol{\mu}_b, \boldsymbol{\Sigma}_{a|b} \mathbf{t} \mathbf{t}^T + \mathbf{R}(t) \boldsymbol{\Sigma}_{bb} \mathbf{R}(t)^T) p(t) dt. \quad (9)$$

Unfortunately, we cannot calculate analytically the integral in Equation 9. To make progress, we proceed in two steps: first, we approximate the integrand with the Gaussian approximation $N(x, t | \mathbf{m}, \mathbf{S})$ by minimising the Kullback-Leibler divergence between them. Secondly, we calculate the Gaussian marginal $N(x | m_x, s_x^2) = \int N(x, t | \mathbf{m}, \mathbf{S}) dt$ which is the approximate support for coordinate x .

⁶ Our method does not rely on this particular choice of prior.

⁷ In practice, we set them to a small value e.g. $\varsigma = \varrho = 10^{-10}$ for numerical stability.

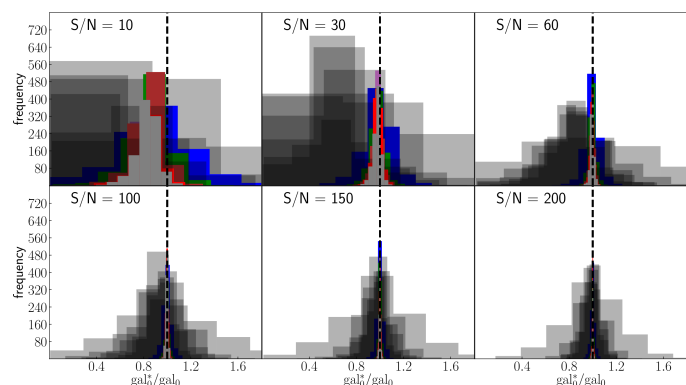


Fig. 3. Recovered FVG host-galaxy fluxes (gal_0^*) for various S/N and time sampling. The distributions obtained for the CS are shown with the same colors as the light curves in Figure 2. For an easy comparison we show in black the distributions obtained for the HS. The FVG applied to the CS appears to be considerably better than the HS; it is characterized by having the smallest dispersion around the true galaxy (gal_0 ; black vertical dotted line) for a $S/N > 100$ (see text).

Hence, the density that describes the distribution of the i -th coordinate of the sought intersection $\mathbf{u}x$ is the Gaussian $N(u_i x | u_i m_x, u_i^2 s_x^2)$. Note, however, that the Gaussian density allows negative values for coordinate x . To avoid this, we work with the reparametrisation $\chi = \sqrt{x}$, i.e. we infer an approximate Gaussian marginal posterior $N(\chi | m_\chi, s_\chi^2)$ for χ instead of x . Consequently, since χ has a Gaussian distribution, coordinate x has a noncentral chi-squared distribution that supports only positive values (Johnson et al. 1995).

Finally, because of the complex probability density of the noncentral chi-squared distribution, we define the density of the i -th coordinate of the sought intersection $\mathbf{u}x$ implicitly as:

$$u_i x = u_i \chi^2, \quad \chi \sim N(\chi | m_\chi, s_\chi^2). \quad (10)$$

3. Simulations

In this section we explore the ability of the FVG, along with our probabilistic reformulation, to recover the host-galaxy contribution under different simulated scenarios. We consider the observational characteristics of PRM campaigns such as time sampling, signal-to-noise (S/N), and the occurrence of time delays in the observed light curves. In particular, we focus on the next future public optical/near-infrared Legacy Survey of Space and Time (LSST), which will monitor about 10 million quasars in six broad-band filters (*ugrizy*) during 10 years of operation.

Our simulation methodology follows Pozo Nuñez et al. (2019). First, we model the driving AGN continuum light curves as a random walk process with a power spectral density $P(\nu) \propto \nu^{-2}$ (Kelly et al. 2009; Caplar et al. 2017). The total emission $L(\text{AGN})_\nu$ from the AGN is then calculated by integrating the Planck function of a black-body,

$$L(\text{AGN})_\nu = 2\pi \int_{r_{\text{in}}}^{r_{\text{out}}} B_\nu(T(r)) r dr \quad (11)$$

where B_ν is characterized by the radial temperature profile of an optically thick geometrically thin accretion disk, $T(r) \propto r^{-3/4}$. The effects of varying disk luminosity as a function of orientation are negligible for the purpose of this work. Consequently, we

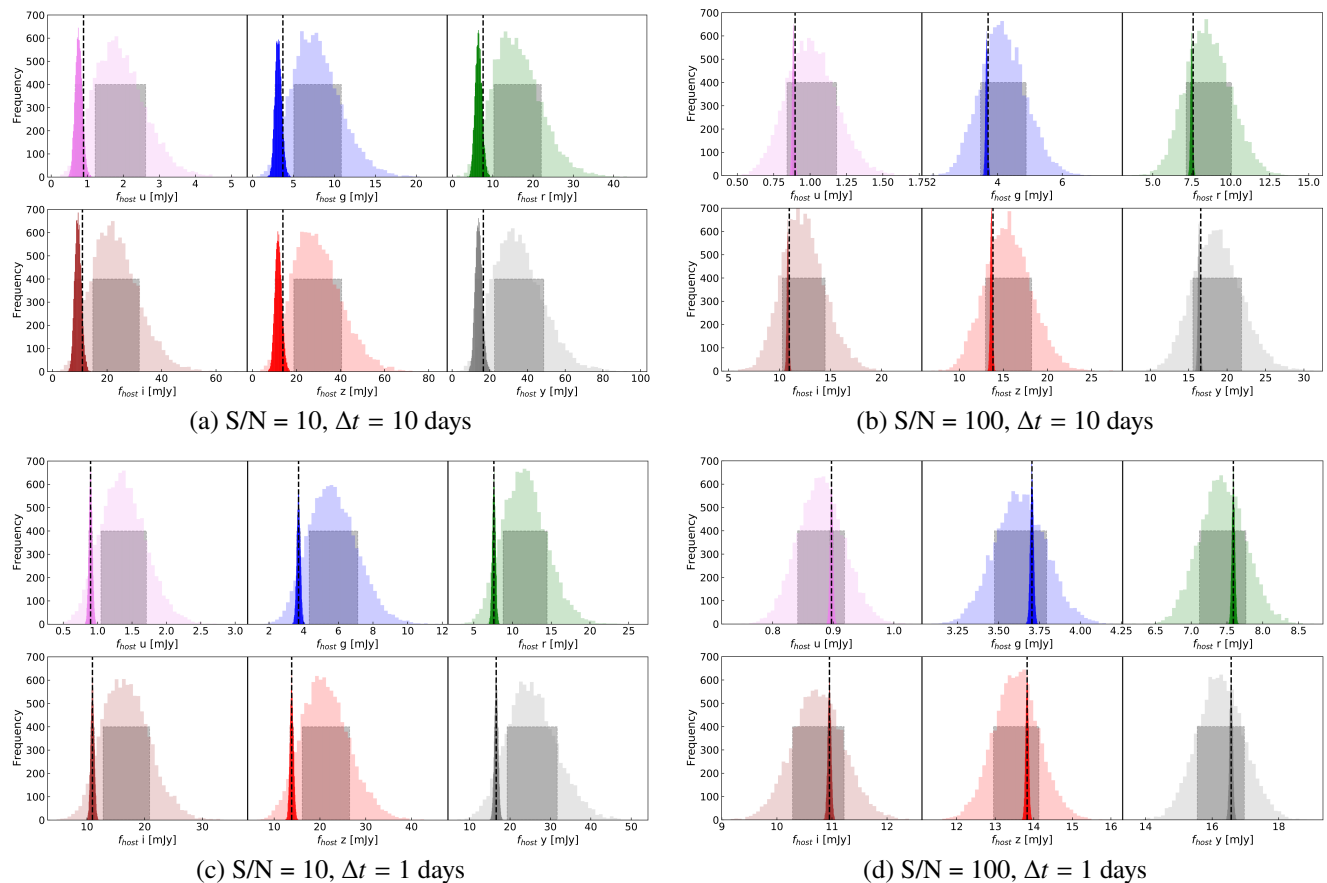


Fig. 4. Recovered PFVG distributions (see Equation 10) of host-galaxy fluxes obtained for the HS (transparent colored histogram) and CS (solid colored histogram). Distributions obtained for poorly sampled light curves, with low and high S/N, are shown in panels (a) and (b), respectively. Distributions obtained for well sampled light curves, with low and high S/N, are shown in panels (c) and (d), respectively. The vertical dotted line marks the true galaxy value used in the simulations (gal_0). The 68% confidence range used to estimate the 1σ uncertainty around the median is shown as black transparent boxes.

assume in Equation 11 a face-on ($i = 0^\circ$) configuration. We then mix the AGN accretion disk emission with the host-galaxy contribution measured from the UV/Optical galaxy templates obtained by Kinney et al. (1996) for different morphology types. Finally, the total observed fluxes are calculated by convolving each model component with the transmission curves of the LSST broad-band filters. In Figure A.1 we show an example of the random walk simulated light curves, AGN accretion disk, and host-galaxy spectrum for an arbitrary local Seyfert galaxy from our mock catalogue.

3.1. The effects of time sampling, signal-to-noise and AGN activity

AGN light curves have a stochastic nature and it is very likely to encounter cases in which either a low or a high level of activity is observed. This combined with the fact that astronomical observations are frequently affected by weather conditions, technical issues, and seasonal gaps, poses significant challenges to the FVG method.

In Figure 2 we present an example that illustrates the impact of the above issues on the traditional FVG analysis. The time sampling, Δt , during the LSST monitoring is expected to be between 2 to 5 days. Thus, the light curves have been randomly sampled with an average sampling of $\Delta t = 3$ days. In this example we adopt a signal-to-noise ratio $S/N = 30$, which cor-

responds to the largest expected photometric noise, in particular, for the u band (at ~ 3 per cent noise level). The left panel shows the light curves depicting two distinct states of AGN activity. A low-state characterized by small variability amplitudes, with fluxes undergoing through a steep decrease of about 40 per cent before reaching a minimum at day 65. Afterward, the flux starts to increase by about the same amplitude (40 per cent) until a maximum is reached at 100 days. This represents the beginning of the higher state of AGN activity. At this point the luminosity has already increased by a magnitude of about 1.5 in all filters. During this state the AGN exhibit a period of stronger variability with light curve features characterized by single outbursts with ~ 10 per cent variability amplitudes, as seen in the range between 140 to 180 days. Those variability events, regulated by both low and high states of AGN activity, are crucial for the performance of the FVG method. This is shown in the FVG diagram in the right panel of Figure 2. In the first test we consider the combined AGN states (hereafter denoted as CS) and perform an OLS bisector linear regression analysis. The bisector method yields a linear gradient of $\Gamma_{ug} = 1.04 \pm 0.02$, which is consistent with $\Gamma_{UB} \sim 1$ derived from observations of Seyfert-1 galaxies (e.g.; Winkler et al. 1992; Sakata et al. 2010). The intersection point (red circle in Figure 2) between the AGN and galaxy slopes gives a host-galaxy flux of $f_u^{\text{host}} = 0.80$ mJy and $f_g^{\text{host}} = 3.31$ mJy. Here the

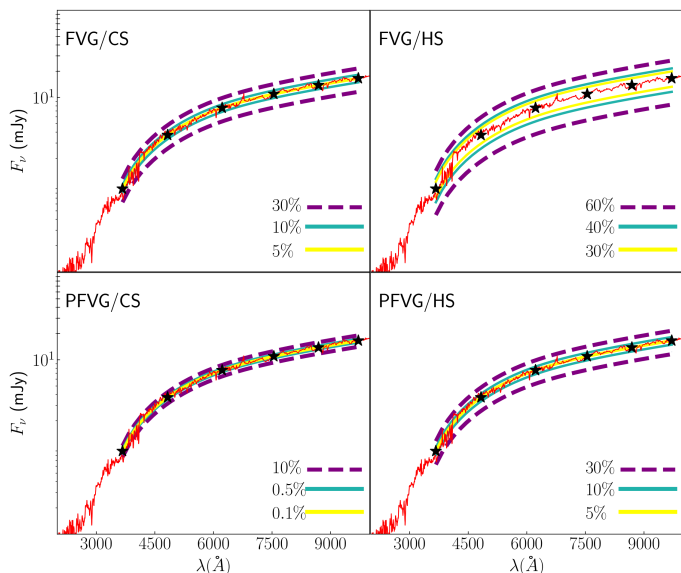


Fig. 5. The precision on the recovered galaxy fluxes obtained from the FVG (upper panels) and PFVG (lower panels) distributions for the CS and HS of AGN activity. The red line shows the Sa-type host-galaxy (observer’s frame) spectrum. The galaxy fluxes (in mJy), at each filter, are plotted as black filled stars. The lines indicate the range of galaxy values recovered within the 68% confidence interval, and are given for a S/N = 10 (purple), 100 (cyan), and 200 (yellow), respectively.

true host-galaxy vector, $\text{gal}_0 = (0.89, 3.70)^8$, obtained from the scaled Sa-type template (Figure A.1), is recovered at 10 and 10.5 per cent precision for u and g -bands, respectively. In the second test we consider only the higher state of AGN activity (hereafter denoted as HS) for which the bisector method yields a linear gradient of $\Gamma_{ug} = 1.13 \pm 0.13$ (orange line). The AGN slope is notably steeper, and with a larger uncertainty, hence leading to a different intersection point ($f_u^{\text{host}} = 1.22$ mJy and $f_g^{\text{host}} = 5.05$ mJy; red diamond), and overestimating the true host-galaxy by about ~ 40 per cent in both u and g -bands, respectively.

To study the performance of the FVG under different observational conditions, we repeat the same analysis for simulated light curves with various S/N ratios (10,30,60,100,150, and 200) and time sampling chosen in the interval $[\Delta t_{\text{min}}, \Delta t_{\text{max}}] = [0.1, 10]$ spaced by 0.01 days. We denote by gal_0^* the estimated host-galaxy vector⁹. The recovered distributions of host-galaxy fluxes, gal_0^* , are shown in Figure 3. We find that the performance of the FVG when applied to the HS is strongly dependent on the quality of the light curves; in particular, FVG appears more sensitive to the presence of noise rather than to time sampling. In the case of S/N < 100, the HS (black histograms) exhibit a broad and asymmetric distribution around the central values, with a systematic bias (up to about 50 per cent) towards small gal_0^* . For higher quality data (i.e., S/N ≥ 100) the distributions are more symmetric and unbiased with $\langle \text{gal}_0^* \rangle \simeq \text{gal}_0$, however, still substantially broader around the mean value. In contrast to the HS, the FVG performance on the CS (colored histograms) becomes less sensitive to the S/N, leading to improved galaxy statistics with a relatively unbiased and narrower distributions of gal_0^* . An exception is seen

⁸ We denote the true galaxy vector by gal_0 , which is represented by the FVG intersection point of the noiseless and ideally sampled light curve ($\Delta t = 0.01$ days), as shown in the Appendix in Figure A.2. The photometric bands implied by gal_0 are made clear by the context.

⁹ As in the definition of gal_0 , the implied photometric bands are made clear by the context.

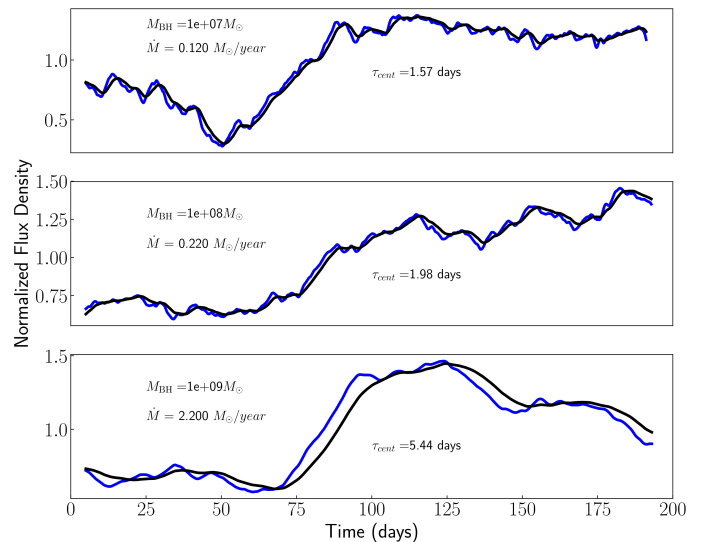


Fig. 6. AD mock light curves with time delays. For illustration, only the u (blue) and y (black) light curves are shown, with the former having the larger delay. The centroid of the transfer function obtained for the y -band with respect to the u -band is labeled inside each panel.

for the lower quality data (i.e., S/N ≤ 30), where a bias (up to about 30 per cent) towards smaller values is still present. For the case of S/N ≥ 100 , the CS distributions becomes narrower and the true galaxy is recovered with 10 per cent precision. Based on these simulations, the recovered precision is consistent with the precision obtained from PRM observational campaigns. We return to this issue in Section 4.

3.1.1. Comparison with proposed PFVG method

We have carried out the PFVG analysis using the same simulated light curves as for the traditional FVG in the previous section. The results are summarized in Figure 4. The PFVG performance on the CS appears to be considerably superior to the traditional FVG, especially for the case of the worst quality data (case-a in Figure 4; S/N=10, $\Delta t = 10$ days); it exhibits a very narrow distribution around the central value, with the true galaxy underestimated by only 15 percent compared to the HS. In this particular case, the HS deviates about twice the true galaxy. The PFVG performance improves substantially already at S/N = 100 (panels b and d) where the HS exhibit a more symmetric distribution with the true galaxy within 1-sigma range. Notably, the CS distributions are significantly narrower and the true galaxy is recovered with an exceptional 0.5% precision. We attribute the good performance of the PFVG to the fact that it accounts for the data measurement errors $\sigma_i(t)$ in its formulation (see Eq. 4). As a consequence, we see that as S/N decreases, the performance of PFVG deteriorates in a ‘graceful’ manner rather than abruptly. A comparison between the recovered FVG and PFVG galaxy fluxes is shown in Figure 5. The PFVG results are summarized in Table A.1.

3.2. PRM light curves with time-delays

Time delays, $\tau_c(\lambda)$, between different UV/Optical continuum bands are a prediction of the AD thermal reprocessing scenario ($\tau_c \propto \lambda^{4/3}$; Collier et al. 1998; Frank et al. 2002; Cackett et al. 2007). The delays are interpreted in terms of the light travel time across different regions of the AD, and have been detected for

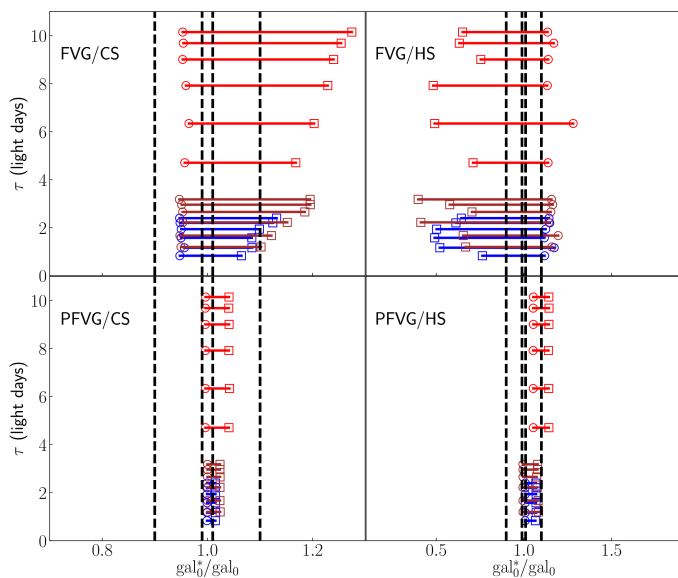


Fig. 7. Distributions of host-galaxy fluxes (gal_0^*) obtained by the FVG (top) and PFVG (bottom) as a function of time-delays. The distributions are shown for each object (in blue, brown, and red) obtained for different S/N, filters, and for a fixed time-sampling $\Delta t = 3$ days. The open circles and squares mark a S/N = 100, and 30, respectively. Dashed inner and outer lines represent 1 and 10% precision, respectively.

a few sources over the past years. The reported measurements are found to be overestimated by factor of ~ 3 than the expected for an optically thick geometrically thin AD (see [Pozo Nuñez et al. 2019](#) and references therein). This overestimation has been attributed mainly to contamination of broad-emission lines into the band-passes, including additional diffuse continuum from the BLR ([Chelouche et al. 2019](#); [Korista, & Goad 2019](#)). Regardless of their magnitude, there is growing evidence that supports their existence in most, if not all, AGN. Whether their production mechanism is exclusively due to AD continuum contribution is a matter of current debate.

In order to quantify any potential biases that might be introduced by PRM light curves with time delays, we generate mock light curves of the continuum based on the AD thermal reprocessing scenario, as outlined in [Pozo Nunez et al. \(2021\)](#). In brief, the observed AD UV/Optical continuum emission, $F_c(\lambda, t)$, is the result of the convolution of the X-ray driving light curve, $F_x(t)$, with a response function $\Psi(\tau|\lambda) \propto \partial B_\nu(\lambda, T(t-\tau))/\partial L_x(t-\tau)$, so that $F_c(\lambda, t) = F_x(t) * \Psi(\tau|\lambda)$, where $\tau \propto (r^2 + h^2)^{1/2}$ is the time delay function for a face-on Keplerian ring/disk structure. The disk is irradiated by a X-ray corona located at a distance h above the plane ([Sergeev et al. 2005](#)) and has a temperature profile, $T(r) \propto (M_{\text{BH}}\dot{M})^{1/4}r^{-3/4}$, given by the standard [Shakura & Sunyaev \(1973\)](#) theory.

We generate the AD mock light curves for three objects with black hole masses $M_{\text{BH}} = 10^7, 10^8, \text{ and } 10^9 M_\odot$, and accretion rates $\dot{M} = 0.12, 0.22, \text{ and } 2.2 M_\odot \text{ yr}^{-1}$, respectively. We assume objects are accreting at 10% Eddington. We use the same random seed as in Figure 2 to create the driving X-ray light curve. The driver is then convolved with transfer functions obtained for each black hole masses and accretion rates. We note that the choice of these model parameters is only for illustrative purposes, allowing the time delay to be large enough to quantify possible biases while neglecting the effects of redshift and galaxy contribution dependency.

Figure 6 shows an example of the simulated AD light curves observed in the u and y -bands. These two bands display the largest difference between them in terms of time delay, as measured by the centroid of the transfer functions. The original light curves have an ideal time sampling of $\Delta t = 0.1$ days, and a time span of 190 days. We add the galaxy contribution, observational noise, and re-sample the light curves in the same way as performed in Section 3.1. The FVG and PFVG are applied on the re-sampled and noisy light curves. The recovered distributions of host-galaxy, gal_0^* , as a function of τ for different bands are shown in Figure 7. The results are shown for a fixed time sampling of $\Delta t = 3$ days, and for a S/N = 30 and 100. The analysis includes both CS and HS cases of AGN activity. We find that the traditional FVG is more sensitive to the presence of time-delays in the light curves; in the CS case, it shows a clear bias towards larger galaxy values, by up to $\sim 20\%$, as the time delay increases and the S/N decreases (open squares). A more stable behaviour is seen for S/N = 100 (open circles), where the galaxy is underestimated by only $\sim 5\%$ of the true value. The opposite behaviour is seen for the HS, case where the galaxy is biased towards smaller values as the S/N decreases. In this case, the galaxy is underestimated by about 50% for a S/N = 30, and overestimated by up to $\sim 15\%$ for a S/N = 100.

As can be seen in the bottom panel of Figure 7, the proposed PFVG method is less sensitive to the presence of time-delays in the light curves, and it clearly outperforms the FVG in CS and HS cases of AGN activity. It shows considerably less biased results and a more stable behaviour per filter. Most notable is the CS case, where the host-galaxy is recovered within ~ 1 and 5% precision for S/N ratios of 100 and 30, respectively. In the HS case, the magnitude of the bias increases up to $\sim 10\%$ of the true value.

4. Data applications

In this section we apply the PFVG method to AGN data obtained by PRM campaigns, and for which host-galaxy estimations have been obtained with the traditional FVG method. We select three sources: Mrk509, Mrk279, and 3C120. The Mrk objects were monitored as part of a narrow-band PRM campaign dedicated to the RM of the accretion disk in AGN ([Pozo Nuñez et al. 2017](#); [Chelouche et al. 2019](#)). The object 3C120 was observed as part of a simultaneous broad-band PRM monitoring of the Broad-line region and the dust torus in AGN ([Ramolla et al. 2018](#)). In the following cases, unless otherwise stated, the candidate host-galaxy vector (denoted by \mathbf{u} in Sect 2.3.2) is given by [Sakata et al. \(2010\)](#). All data are publicly available and can be retrieved directly from the respective journals.

4.1. Mrk509

Mrk509 is a nearby ($z = 0.0344$; [Huchra et al. 1993](#)) and bright ($V = 13$ mag) Seyfert 1 galaxy known for its strong variability and characteristics outflows ([Kaastra et al. 2011](#)). Through the modeling of high-resolution Hubble Space Telescope (HST) images, [Bentz et al. \(2009\)](#) found a host-galaxy profile consistent with a bulge morphology type. These results are in agreement with the host-galaxy fluxes derived by the traditional FVG analysis presented in [Pozo Nuñez et al. 2019](#) (PN+2019). Here we analyze the photometric light curves obtained in two different epochs (2016/2017) using the narrow-bands with central wavelengths at $4300 \pm 50, 5700 \pm 50, 6200 \pm 60, \text{ and } 7000 \pm 60 \text{ \AA}$ respectively. The quality of the light curves obtained during both epochs are

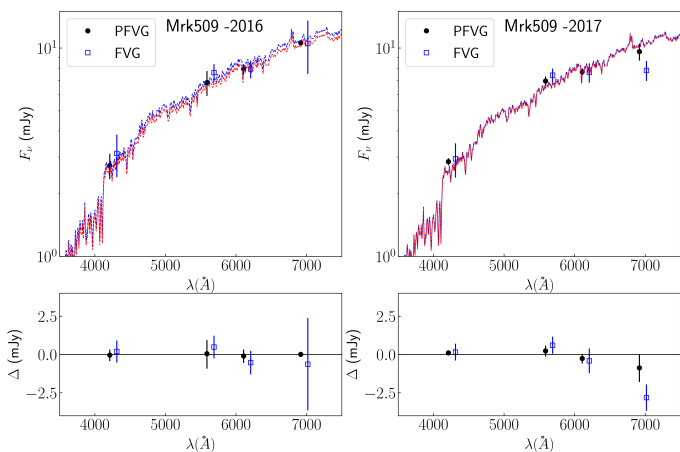


Fig. 8. Application of the PFVG method to the object Mrk509 for epochs 2016 (left) and 2017 (right). The black dots correspond to the median of the recovered distributions of host galaxy fluxes (See Appendix A.4). The error bars show the formal 1σ uncertainty around the median. The results obtained by the FVG are shown with blue open squares. The redshifted bulge galaxy template of Kinney et al. 1996 is fitted to both PFVG (red) and FVG (blue) host-galaxy fluxes. The fit residuals, as obtained for the PFVG and FVG, are shown in the bottom panels. A small wavelength shift between the PFVG and FVG was introduced for clarity.

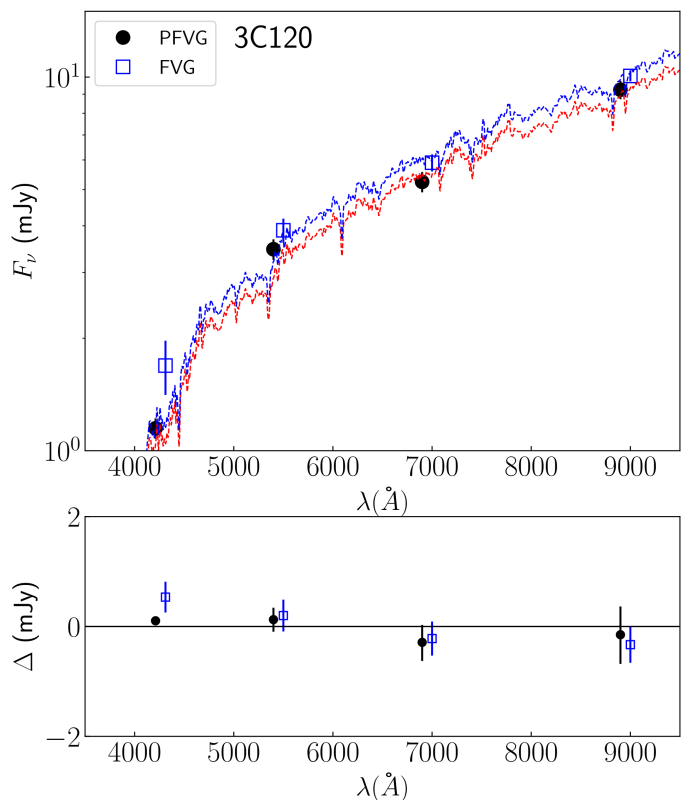


Fig. 10. Same as Figure 8 but for 3C120, and a redshifted S0 galaxy template of Kinney et al. 1996 (red and blue lines).

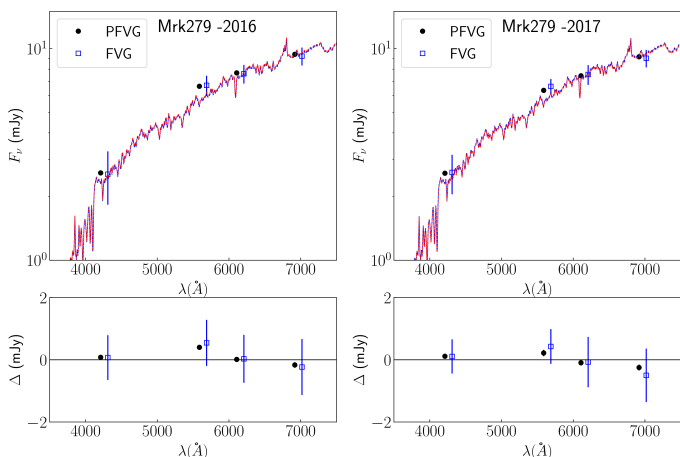


Fig. 9. Same as Figure 8 but for Mrk279, and a redshifted Sa galaxy template of Kinney et al. 1996 (red and blue lines).

similar, with an average sampling of 1 day, and $S/N \sim 150$ for each photometric band. Figure 8 shows the PFVG results along with the FVG obtained by PN+2019. As in PN+2019, we adopted the host-galaxy color given by Sakata et al. (2010). The recovered PFVG distributions are shown in the Appendix A.4. Overall, the results obtained for 2016 and 2017 are consistent, as expected, given the high quality of the light curves. The PFVG is able to recover the galaxy fluxes with 10% precision compared to 20% obtained by the traditional FVG method. These new results lead to a better match to the bulge galaxy template, as can be seen in the fit residuals at the bottom panel of Figure 8. Deviations from the assumptions of the linear relationship between the fluxes (Equation 2) due to the accretion disk time delays observed in Mrk509 (PN+2019) are negligible ($< 1\%$).

4.2. Mrk279

Mrk279 is a nearby ($z = 0.031$) low luminosity ($V = 15$ mag) Seyfert 1 galaxy. FVG analysis by Chelouche et al. 2019 revealed a S0/Sa host-galaxy morphology, in agreement with the results obtained through modeling of high-resolution HST images (Pogge & Martini 2002). The PFVG is able to recover the galaxy fluxes with an exceptional 1% precision compared to 30% obtained by the traditional FVG method (Figure 9). As shown in the Appendix A.4, the average S/N of the light curves is ~ 90 . This is considerably lower than the average $S/N \sim 150$ obtained for Mrk509, but consistent with the fact that Mrk279 is about 50% less luminous. Just as we remarked in the simulations in Section 3.1.1, we attribute the superior performance of the PFVG to the fact that it explicitly accounts for errors in the measurements.

4.3. 3C120

3C120 is a nearby Fanaroff-Riley Class I radio galaxy at redshift $z = 0.033$ (Walker et al. 1987). It has often been the target of several RM campaigns due to its strong variability, with amplitudes of up to ~ 2 mag on timescales of a few years (Sakata et al. 2010; Pozo Nuñez et al. 2012; Grier et al. 2012). More recently, Ramolla et al. (2018) (R+2018) carried out a PRM campaign in order to study both the BLR and the dust torus. R+2018 used the Johnson B and V -broad bands to estimate the AGN continuum emission, and the R and I -broad bands to estimate the fraction of continuum underneath the $H\alpha$ emission line. The FVG analysis by R+2018 was performed using the BVI -bands. The host-galaxy contribution in the R -band was not recovered by the FVG due to the contamination of the $H\alpha$ emission line, which is about 14 per cent of the total flux. Moreover, deviations from the linear relationship between the fluxes (Equation 2) were noted since the

R -band contains the delayed $H\alpha$ emission, and which does not correlate with the continuum variations traced by the other bands. To overcome these issues, R+2018 fitted the spectral energy distribution (SED) with a redshifted S0 (Bentz et al. 2009) galaxy template and recovered an R -band galaxy flux of 5.90 ± 0.30 mJy.

Following R+2018, we adopted a host-galaxy color given by a S0 template (Kinney et al. 1996). The results are shown in Figure 10. Notably, the recovered R -band galaxy flux 5.24 ± 0.32 mJy is in full agreement with the SED value reported by R+2018. Previous knowledge of the true color of the host-galaxy provides an important advantage to the proposed PFVG method, hence the R -band galaxy flux can be directly recovered from the observed light curves. This is possible since the PFVG estimates a density of likely host-galaxy vectors along the assumed host-galaxy line. Therefore, in this particular case, the method is similar to searching for the best fit in a traditional SED analysis but with the advantage of using the full information from the observed light curves.

Overall our results for 3C120 are consistent with those derived from the FVG method, except for the B -band where the PFVG flux is about 1.5 smaller than the reported FVG value 1.69 ± 0.28 by R+2018. The PFVG shows a very narrow distribution of fluxes (see Appendix A.5) with a median value of 1.15, and a 1σ uncertainty of 6% compared to 16% obtained by the traditional FVG. The median of the PFVG distribution is, however, in better agreement with the S0 host-galaxy spectrum shown in Figure 10. The better performance of the PFVG is expected, since the B -band corresponds to the light curve with the lowest $S/N = 46$. As shown in the simulations in Section 3.1, if the noise level differs considerably from band to band, then the PFVG method will outperform the FVG, as it weighs data items according to their noise measurement.

5. Summary and conclusions

We have presented a novel Probabilistic Flux Variation Gradient approach to disentangle the AGN and host-galaxy contributions in the context of photometric reverberation mapping of AGN. We studied its performance using simulated light curves of varying quality, in particular, focusing on the observational characteristics of the next LSST survey. We have demonstrated that by explicitly accounting for error measurements in the light curves, the new probabilistic approach outperforms the traditional FVG in all simulated observational scenarios explored in this work. This leads to recovered galaxy fluxes with less than 1% precision for light curves with moderate S/N . This represents a significant improvement compared to the 20% precision obtained by the traditional FVG.

Unlike the traditional FVG, PFVG does not identify just a single line that goes through the given total fluxes, but rather a density of possible lines. This makes it more robust to the presence of noise and informs us of the uncertainty in our estimates.

Both FVG and PVFG assume that the total flux observations form a line in the space of all filters (see Section 2). Both assume that the only reason that observations may deviate from this line is due to noise. In reality, however, total flux observations may additionally deviate from this line due to the presence of time-delays, e.g. originated in the AGN accretion disk or broad-line region. This can lead to galaxy measurements which are biased by less than 5% in the case of objects with small to moderate black hole masses. The biases can reach up to 10% in the case of the largest black hole masses (~ 6 days time-delay). In view of the overall measurements errors, of typically more than 10%

introduced by the absolute calibration of the photometric data, any bias in the PFVG galaxy estimation appears to be negligible.

The application of the PFVG to PRM data sets yielded host-galaxy fluxes which are in better agreement with the host-galaxy morphology types obtained through the modeling of high-resolution images. As a consequence, the method enables reliable estimates of the pure AGN luminosity, necessary to probe theoretical models of the AGN accretion disk, broad-line region and dust-torus structure. This is specially important considering the large amount of data that will be provided by future large photometric survey telescopes like the LSST.

In future endeavours we would like to address certain assumptions made in the formulation of the proposed PVFG: currently we assume that observational noise is Gaussian distributed but other choices may be more appropriate especially in the presence of outliers. Moreover, we assume that no observations are missing and that observations in different filters co-occur (i.e. they are observed at the same time instance) so that we can form vectors of them. This is a limitation that prevents PFVG from combining observations from different surveys, as each survey typically has its own observational characteristics (e.g. monitoring schedules, cadence).

Finally, an implementation of our method is publicly available through as a *Julia* package at <https://github.com/HITS-AIN/ProbabilisticFluxVariationGradient.jl>.

Acknowledgements. The authors gratefully acknowledge the generous and invaluable support of the Klaus Tschira Foundation. This research has made use of the NASA/IPAC Extragalactic Database (NED) which is operated by the Jet Propulsion Laboratory, California Institute of Technology, under contract with the National Aeronautics and Space Administration. This research has made use of the SIMBAD database, operated at CDS, Strasbourg, France.

References

- Amendola, L., Appleby, S., Avgoustidis, A., et al. 2018, *Living Reviews in Relativity*, 21, 2
- Bentz, M. C., Peterson, B. M., Netzer, H., et al. 2009, *ApJ*, 697, 160. doi:10.1088/0004-637X/697/1/160
- Bentz, M. C., Denney, K. D., Grier, C. J., et al. 2013, *ApJ*, 767, 149
- Bettoni, D., Falomo, R., Kotilainen, J. K., et al. 2015, *MNRAS*, 454, 4103. doi:10.1093/mnras/stv2233
- Bishop CM (1999a) Bayesian pca. In: Kearns MJ, Solla SA, Cohn DA (eds) *Advances in Neural Information Processing Systems 11*, MIT Press, pp 382–388
- Bishop CM (1999b) Variational principal components. In: *Proceedings Ninth International Conference on Artificial Neural Networks, ICANN'99*, IEE, vol 1, pp 509–514
- Cackett, E. M., Horne, K., & Winkler, H. 2007, *MNRAS*, 380, 669
- Caplar, N., Lilly, S. J., & Trakhtenbrot, B. 2017, *ApJ*, 834, 111
- Chelouche D., Pozo Nuñez F., Kaspi S., 2019, *NatAs*, 3, 251
- Choloniewski, J. 1981, *Acta Astron.*, 31, 293
- Collier, S. J., Horne, K., Kaspi, S., et al. 1998, *ApJ*, 500, 162
- Falomo, R., Bettoni, D., Karhunen, K., et al. 2014, *MNRAS*, 440, 476. doi:10.1093/mnras/stu283
- Frank, J., King, A., & Raine, D. J. 2002, *Accretion Power in Astrophysics*
- Gabor, J. M., Impey, C. D., Jahnke, K., et al. 2009, *ApJ*, 691, 705. doi:10.1088/0004-637X/691/1/705
- Glass, I. S. 1997, *MNRAS*, 292, L50. doi:10.1093/mnras/292.1.L50
- Glass, I. S. 1998, *MNRAS*, 297, 18. doi:10.1046/j.1365-8711.1998.01429.x
- Glass, I. S. 2004, *MNRAS*, 350, 1049. doi:10.1111/j.1365-2966.2004.07712.x
- Grier, C. J., Peterson, B. M., Pogge, R. W., et al. 2012, *ApJ*, 755, 60. doi:10.1088/0004-637X/755/1/60
- Huchra, J., Latham, D. W., da Costa, L. N., Pellegrini, P. S., & Willmer, C. N. A. 1993, *AJ*, 105, 1637
- Isobe, T., Feigelson, E. D., Akritas, M. G., et al. 1990, *ApJ*, 364, 104. doi:10.1086/169390
- Johnson, N. L., Kotz, S., Balakrishnan, N., 1995, *Continuous univariate distributions*, volume 2
- Jenkins, J. M., Tenenbaum, P., Caldwell, D. A., et al. 2018, *Research Notes of the American Astronomical Society*, 2, 47
- Kaastra, J. S., Petrucci, P.-O., Cappi, M., et al. 2011, *A&A*, 534, A36.

- Kelly, B. C., Bechtold, J., & Siemiginowska, A. 2009, *ApJ*, 698, 895
- Kinney, A. L., Calzetti, D., Bohlin, R. C., et al. 1996, *ApJ*, 467, 38
- Kollmeier, J., Anderson, S. F., Blanc, G. A., et al. 2019, *BAAS*51, 274
- Korista, K. T., & Goad, M. R. 2019, *MNRAS*, 489, 5284
- Koshida, S., Minezaki, T., Yoshii, Y., et al. 2014, *ApJ*, 788, 159.
doi:10.1088/0004-637X/788/2/159
- LSST Science Collaboration, Abell, P. A., Allison, J., et al. 2009, arXiv e-prints, [arXiv:0912.0201](https://arxiv.org/abs/0912.0201)
- Mehdipour, M., Kaastra, J. S., Kriss, G. A., et al. 2015, *A&A*, 575, A22.
doi:10.1051/0004-6361/201425373
- Natarajan, P., Pacucci, F., Ferrara, A., et al. 2017, *ApJ*, 838, 117
- Oknyanskij, V. L. 1999, *Odessa Astronomical Publications*, 12, 99
- Pierce, C. M., Lotz, J. M., Primack, J. R., et al. 2010, *MNRAS*, 405, 718.
doi:10.1111/j.1365-2966.2010.16502.x
- Pogge, R. W. & Martini, P. 2002, *ApJ*, 569, 624. doi:10.1086/339400
- Pović, M., Sánchez-Portal, M., Pérez García, A. M., et al. 2012, *A&A*, 541, A118.
doi:10.1051/0004-6361/201117314
- Pozo Nuñez, F., Ramolla, M., Westhues, C., et al. 2012, *A&A*, 545, A84
- Pozo Nuñez, F., Westhues, C., Ramolla, M., et al. 2013, *A&A*, 552, A1
- Pozo Nuñez, F., Haas, M., Chini, R., et al. 2014, *A&A*, 561, L8. doi:10.1051/0004-6361/201323178
- Pozo Nuñez, F., Ramolla, M., Westhues, C., et al. 2015, *A&A*, 576, A73.
doi:10.1051/0004-6361/201525910
- Pozo Nuñez, F., Chelouche, D., Kaspi, S., & Niv, S. 2017, *PASP*, 129, 094101
- Pozo Nuñez, F., Gianniotis, N., Blex, J., et al. 2019, *MNRAS*, 490, 3936
- Ramolla, M., Pozo Nuñez, F., Westhues, C., et al. 2015, *A&A*, 581, A93.
doi:10.1051/0004-6361/201526846
- Ramolla, M., Haas, M., Westhues, C., et al. 2018, *A&A*, 620, A137.
doi:10.1051/0004-6361/201732081
- Sakata, Y., Minezaki, T., Yoshii, Y., et al. 2010, *ApJ*, 711, 461. doi:10.1088/0004-637X/711/1/461
- Sergeev, S. G., Doroshenko, V. T., Golubinskiy, Y. V., Merkulova, N. I., & Sergeeva, E. A. 2005, *ApJ*, 622, 129
- Shakura, N. I., & Sunyaev, R. A. 1973, *A&A*, 24, 337
- Suganuma, M., Yoshii, Y., Kobayashi, Y., et al. 2006, *ApJ*, 639, 46.
doi:10.1086/499326
- Michael E Tipping and Christopher M Bishop. Probabilistic principal component analysis. *Journal of the Royal Statistical Society: Series B (Statistical Methodology)*, 61(3):611–622, 1999.
- Vazquez, B., Galianni, P., Richmond, M., et al. 2015, *ApJ*, 801, 127.
doi:10.1088/0004-637X/801/2/127
- Villforth, C., Hamann, F., Rosario, D. J., et al. 2014, *MNRAS*, 439, 3342.
doi:10.1093/mnras/stu173
- Watson, D., Denney, K. D., Vestergaard, M., et al. 2011, *ApJ*, 740, L49
- Walker, R. C., Benson, J. M., & Unwin, S. C. 1987, *ApJ*, 316, 546.
doi:10.1086/165225
- Winkler, H., Glass, I. S., van Wyk, F., et al. 1992, *MNRAS*, 257, 659.
doi:10.1093/mnras/257.4.659

Appendix A:

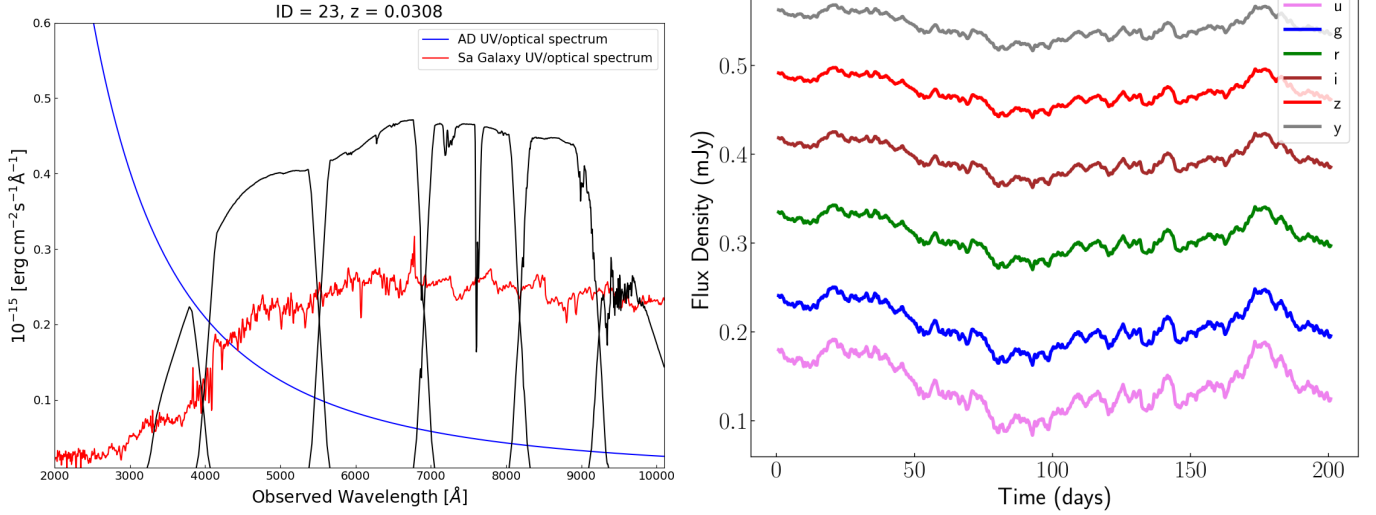


Fig. A.1. Left panel – example of a simulated UV/Optical AGN spectrum (blue solid line) along with a Sa-type host-galaxy template (red solid line). The transmission curves of the LSST broad-band filters are shown with solid black lines (*ugrizy*; from left to right). In this particular case the host-galaxy contributes about 50% of the total flux at 5100Å (rest frame). Right panel – Flux calibrated light curves resulting from the convolution between each LSST broad-band filter with the AGN and galaxy components.

Table A.1. PFVG results.

Filter	gal ₀	S/N = 10, Δt = 10		S/N = 100, Δt = 10		S/N = 10, Δt = 1		S/N = 100, Δt = 1	
		CS/HS		CS/HS		CS/HS		CS/HS	
<i>u</i>	0.897	0.76 ^{+0.10} / _{-0.10}	1.85 ^{+0.63} / _{-0.77}	0.89 ^{+0.01} / _{-0.01}	1.01 ^{+0.16} / _{-0.18}	0.90 ^{+0.03} / _{-0.03}	1.36 ^{+0.32} / _{-0.35}	0.897 ^{+0.003} / _{-0.003}	0.879 ^{+0.038} / _{-0.039}
<i>g</i>	3.703	3.14 ^{+0.40} / _{-0.43}	7.66 ^{+2.62} / _{-3.18}	3.66 ^{+0.04} / _{-0.04}	4.14 ^{+0.67} / _{-0.75}	3.71 ^{+0.11} / _{-0.11}	5.63 ^{+1.31} / _{-1.49}	3.704 ^{+0.010} / _{-0.010}	3.631 ^{+0.156} / _{-0.162}
<i>r</i>	7.589	6.46 ^{+0.83} / _{-0.88}	15.62 ^{+5.35} / _{-6.42}	7.50 ^{+0.07} / _{-0.07}	8.50 ^{+1.36} / _{-1.54}	7.60 ^{+0.22} / _{-0.22}	11.52 ^{+2.74} / _{-2.94}	7.589 ^{+0.021} / _{-0.022}	7.433 ^{+0.317} / _{-0.332}
<i>i</i>	10.954	9.32 ^{+1.22} / _{-1.28}	22.52 ^{+7.75} / _{-9.30}	10.82 ^{+0.10} / _{-0.11}	12.24 ^{+1.97} / _{-2.23}	10.96 ^{+0.31} / _{-0.33}	16.63 ^{+3.82} / _{-4.24}	10.954 ^{+0.032} / _{-0.032}	10.742 ^{+0.458} / _{-0.478}
<i>z</i>	13.827	11.74 ^{+1.49} / _{-1.61}	28.54 ^{+9.74} / _{-11.96}	13.65 ^{+0.13} / _{-0.13}	15.53 ^{+2.55} / _{-2.69}	13.84 ^{+0.39} / _{-0.41}	20.96 ^{+4.83} / _{-5.52}	13.827 ^{+0.040} / _{-0.040}	13.549 ^{+0.592} / _{-0.585}
<i>y</i>	16.571	14.08 ^{+1.84} / _{-1.90}	34.32 ^{+11.82} / _{-14.33}	16.37 ^{+0.16} / _{-0.16}	18.59 ^{+3.04} / _{-3.29}	16.58 ^{+0.47} / _{-0.49}	25.12 ^{+5.85} / _{-6.56}	16.570 ^{+0.047} / _{-0.049}	16.247 ^{+0.696} / _{-0.719}

Notes: gal₀ correspond to the true galaxy vector used in the simulations. CS and HS correspond to the results obtained for the AGN combined state higher states of activity, respectively. All fluxes are given in mJy.

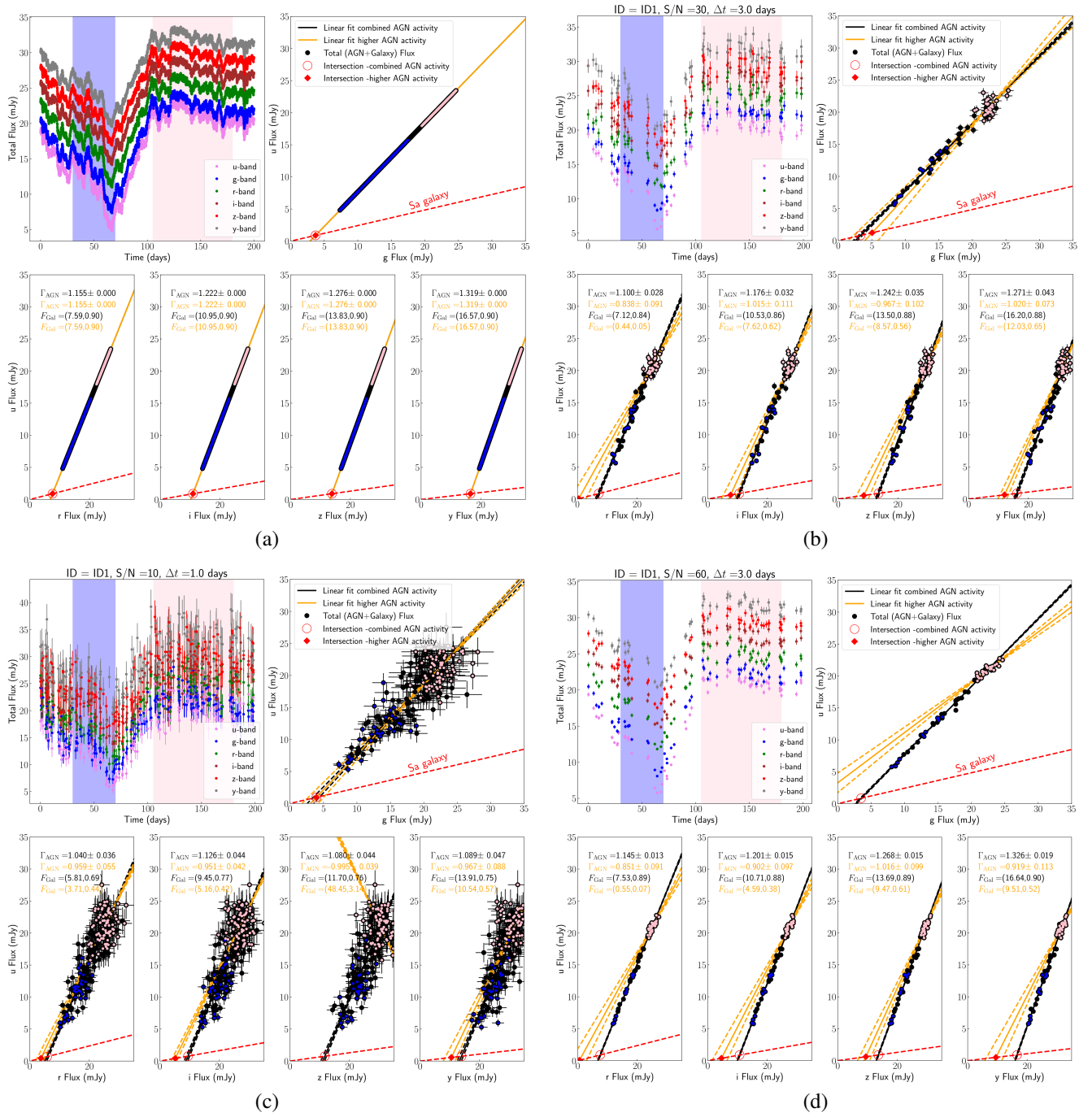


Fig. A.2. FVG for the LSST simulated light curves from our mock catalogue. Panel (a) shows the FVG results obtained for the ideal noiseless light curve with a time sampling of 0.1 days. Panels (b), (c), and (d) shows the FVG results for light curves of varying quality.

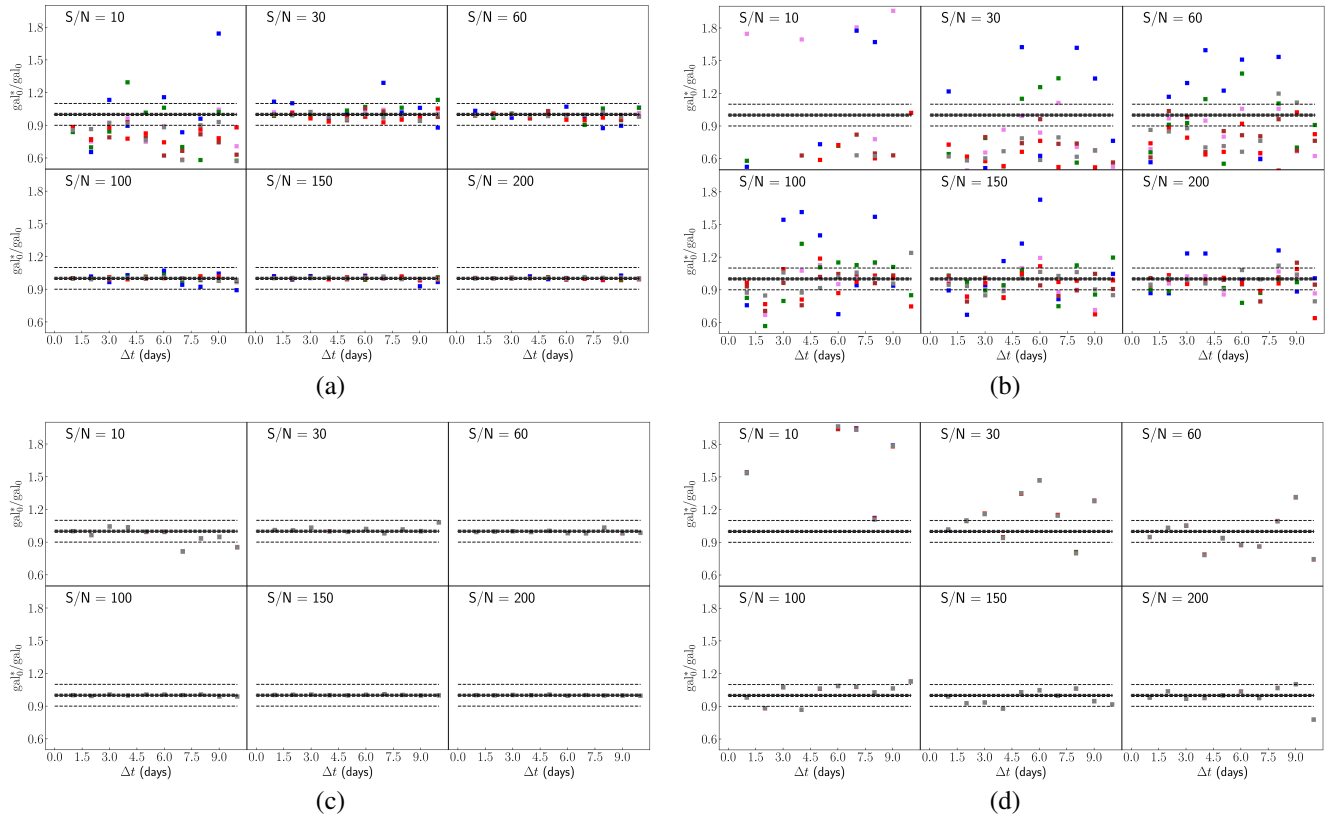


Fig. A.3. Recovered FVG (top) and PFVG (bottom) distributions of host-galaxy fluxes (gal_0^*) for different S/N and time sampling. The left and right panels shows gal_0^* obtained for the CS and HS, respectively.

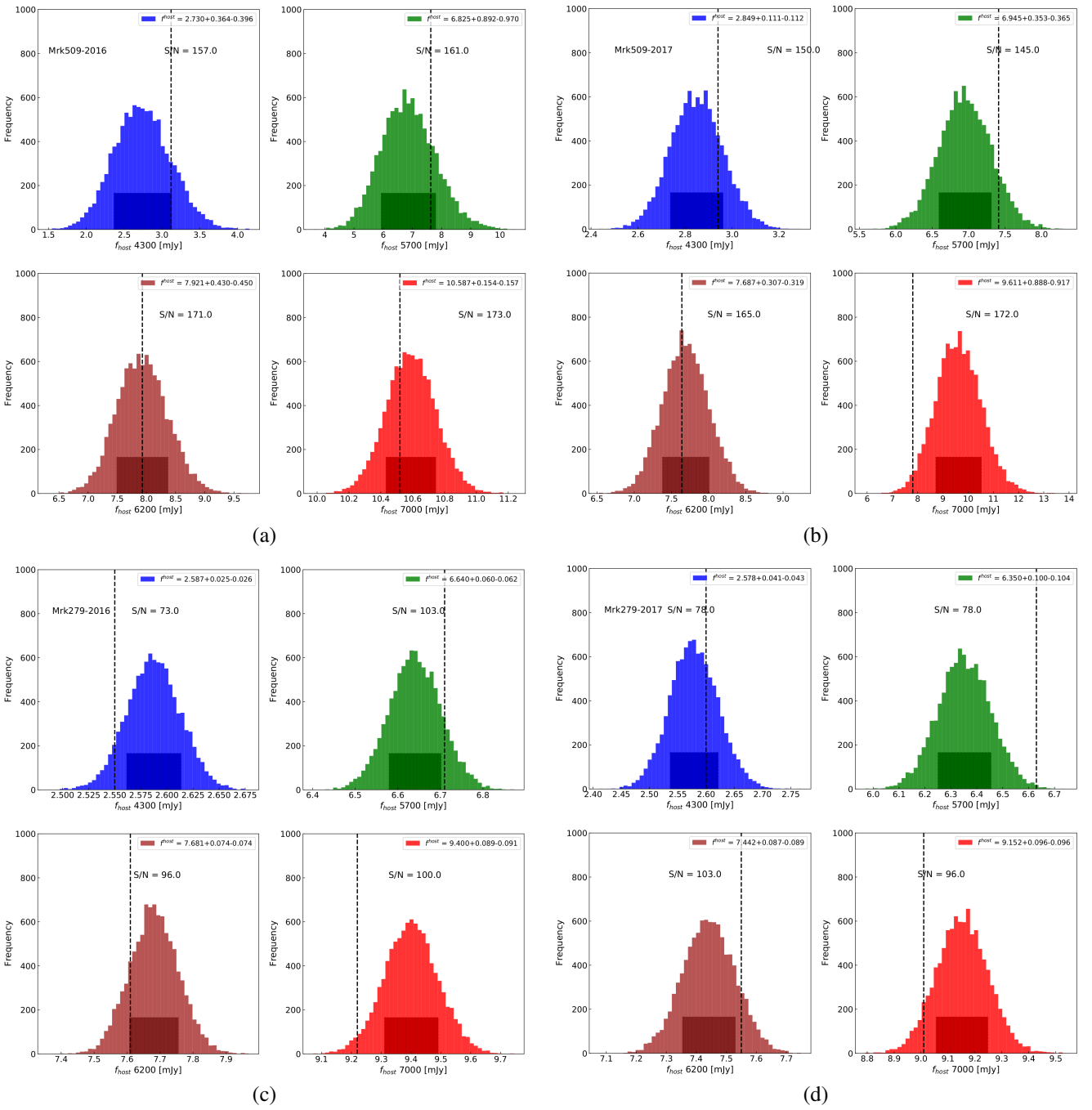


Fig. A.4. Recovered PFVG distributions of host-galaxy fluxes for objects Mrk509 (top panels) and Mrk279 (bottom panels). The vertical dotted line marks the galaxy flux obtained by the FVG method. The dark shaded area marks the 68% confidence range used to estimate the 1σ uncertainty around the median of the distribution.

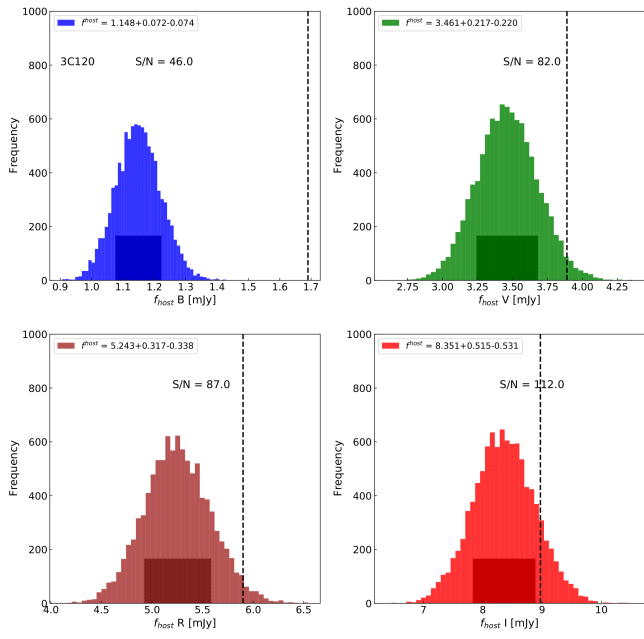


Fig. A.5. Same as Figure A.4 but for 3C120.